Tunable flux through a synthetic Hall tube of neutral fermions

Xi-Wang Luo [1], Jing Zhang,[2,3,*] and Chuanwei Zhang[1,*]

[1]*Department of Physics, The University of Texas at Dallas, Richardson, Texas 75080-3021, USA*

[2]*State Key Laboratory of Quantum Optics and Quantum Optics Devices, Institute of Opto-Electronics, Shanxi University, Taiyuan 030006, P. R. China*

[3]*Synergetic Innovation Center of Quantum Information and Quantum Physics, University of Science and Technology of China, Hefei, Anhui 230026, P. R. China*

(Received 20 April 2020; accepted 7 December 2020; published 22 December 2020)

A Hall tube with a tunable flux is an important geometry for studying quantum Hall physics, but its experimental realization in real space is still challenging. Here we propose to realize a synthetic Hall tube with tunable flux in a one-dimensional optical lattice with the synthetic ring dimension defined by atomic hyperfine states. We investigate the effects of the flux on the system topology and study its quench dynamics. Utilizing the tunable flux, we show how to realize topological charge pumping, where interesting charge flow and transport are observed in rotated spin basis. Finally, we show that the recently observed quench dynamics in a synthetic Hall tube can be explained by the random flux existing in the experiment.

DOI: 10.1103/PhysRevA.102.063327

I. INTRODUCTION

Ultracold atoms are emerging as a promising platform for the study of condensed-matter physics in a clean and controllable environment [1,2]. The capability of generating artificial gauge fields and spin-orbit coupling using light-matter interaction [3–18] offers a new opportunity for exploring topologically nontrivial states of matter [19–25] . One recent notable achievement was the realization of a Harper-Hofstadter Hamiltonian, an essential model for quantum Hall physics, using laser-assisted tunneling for generating artificial magnetic fields in two-dimensional (2D) optical lattices [26–28]. Moreover, a synthetic lattice dimension defined by atomic internal states [29–38] provides a new powerful tool for engineering new high-dimensional quantum states of matter with versatile boundary manipulation [32,33] using a low-dimensional physical system.

Nontrivial lattice geometries with periodic boundaries (such as a torus or tube) allow the study of many interesting physics, such as the Hofstadter's butterfly [39] and Thouless pump [40–45], where the flux through the torus or tube is crucially important. In a recent experiment [37], a synthetic Hall tube has been realized in a one-dimensional (1D) optical lattice and interesting quench dynamics have been observed, where the flux effect was not considered. More importantly, the flux through the tube, determined by the relative phase between Raman lasers, is spatially nonuniform and random for different iterations of the experiment, yielding major deviation from the theoretical prediction. The physical significance and experimental progress raise two natural questions: Can the flux through the synthetic Hall tube be controlled and tuned in realistic experiments? If so, can such controllability lead to the observation of interesting quench dynamics?

In this paper we address these important questions by proposing a simple scheme to realize a controllable flux Φ through a three-leg synthetic Hall tube and studying its quench dynamics and topological pumping. Our main results are:

(i) We use three hyperfine ground spin states, each of which is dressed by one far-detuned Raman laser, to realize the synthetic ring dimension of the tube. The flux Φ can be controlled simply by varying the polarizations of the Raman lasers [11]. The scheme can be applied to both Alkali (e.g., potassium) [11–15] and Alkaline-earth(-like) atoms (e.g., strontium, ytterbium) [46].

(ii) The three-leg Hall tube is characterized as a 2D topological insulator, with Φ playing the role of the momentum along the synthetic dimension. The system also belongs to a 1D topological insulator at $\Phi = 0$ and π, where the winding number is quantized and protected by a generalized inversion symmetry.

(iii) The tunable Φ allows the experimental observation of topological charge pumping in the tube geometry, which also probes the system topology. Interesting charge flow and transport can be observed in a rotated spin basis.

(iv) We study the quench dynamics with a tunable flux and show that the experimental observed quench dynamics in [37] can be better understood using a random flux existing in the experiment.

II. THE MODEL

We consider an experimental setup with cold atoms trapped in 1D optical lattices along the x direction, where transverse dynamics are suppressed by deep optical lattices, as shown in Fig. 1(a). The bias magnetic field is along the z direction to define the quantization axis. Three far-detuned Raman laser fields $\vec{\mathcal{E}}_s$, propagating in the x-y plane, are used to couple

*Corresponding authors: jzhang74@sxu.edu.cn; chuanwei.zhang@utdallas.edu

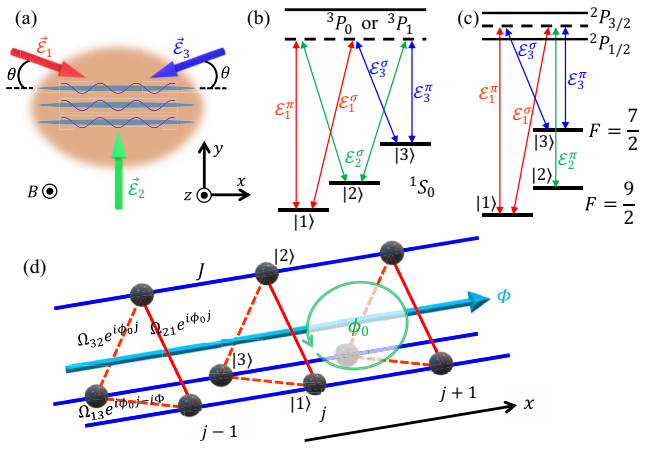

FIG. 1. (a) Schematic of the experimental setup for tunable flux through the synthetic Hall tube. The Raman lasers $\vec{\mathcal{E}}_1$, $\vec{\mathcal{E}}_2$, and $\vec{\mathcal{E}}_3$ generate the couplings along the synthetic dimension spanned by atomic hyperfine states. (b), (c) The corresponding Raman transitions for alkaline-earth(-like) atoms and alkali, respectively. (d) Synthetic Hall tube with a uniform flux ϕ_0 on each side plaquette and Φ through the tube.

three atomic hyperfine ground spin states, with each state dressed by one Raman laser, as shown in Figs. 1(b) and 1(c) for alkaline-earth(-like) (e.g., strontium, ytterbium) and alkali (e.g., potassium) atoms, respectively. The three spin states form three legs of the synthetic tube system as shown in Fig. 1(d), and the tight-binding Hamiltonian is written as

$$H = \sum_{j;s\neq s'} \widetilde{\Omega}_{ss';j} c^\dagger_{j,s} c_{j,s'} - \sum_{j;s} (J c^\dagger_{j,s} c_{j+1,s} + \text{H.c.}), \quad (1)$$

where $\widetilde{\Omega}_{ss';j} = \Omega_{ss'} e^{i\phi_{j;ss'}}$, $c^\dagger_{j,s}$ is the creation operator with j, and s the site and spin index. J and $\Omega_{ss'}$ are the tunneling rate and Raman coupling strength, respectively. For alkaline-earth(-like) atoms, we use three states in the $^1S_0$ ground manifold to define the synthetic dimension. The long lifetime $^3P_0$ or $^3P_1$ levels are used as the intermediate states for the Raman process [see Fig. 1(b)] such that the $\delta m_F = \pm 2$ Raman process does not suffer heating issues [36]. For alkaline atoms [see Fig. 1(c)] we choose three hyperfine spin states $|F, m_F\rangle$, $|F, m_F - 1\rangle$, and $|F - 1, m_F\rangle$ from the ground-state manifold to avoid the $\delta m_F = \pm 2$ Raman process, so that far-detuned Raman lasers tuned between the $D1$ and $D2$ lines can be used to reduce the heating [11,12].

The laser configuration in Fig. 1(a) generates a uniform magnetic flux penetrating each side plaquette as well as a tunable flux through the tube. Each Raman laser may contain both z polarization (responsible for π transition) and in-plane-polarization (responsible for σ transition) components, which can be written as $\vec{\mathcal{E}}_s = \hat{\mathbf{e}}_\pi \mathcal{E}^\pi_s + \hat{\mathbf{e}}_\sigma \mathcal{E}^\sigma_s$. For alkaline-earth(-like) atoms, we choose $\mathcal{E}^\pi_2 = 0$ so that $\widetilde{\Omega}_{21;j} \propto \mathcal{E}^\pi_1 \mathcal{E}^{\sigma *}_2$, $\widetilde{\Omega}_{32;j} \propto \mathcal{E}^\sigma_2 \mathcal{E}^{\pi *}_3$, and $\widetilde{\Omega}_{13;j} \propto \mathcal{E}^\sigma_3 \mathcal{E}^{\sigma *}_1$. Therefore the corresponding Raman coupling phases are $\phi_{j;21} = (\mathbf{k}_1 - \mathbf{k}_2) \cdot \mathbf{x}_j + \varphi^\pi_1 - \varphi^\sigma_2$, where $\mathbf{k}_s$ is the wave vector of the sth Raman laser, $\varphi^{\pi,\sigma}_s$ are the (π, σ)-component phases of the sth Raman laser at site $j = 0$, and $\mathbf{x}_j = j d_x \hat{\mathbf{x}}$ is the position of site j with d_x the lattice constant. As a result, we have $\phi_{j;21} = j\phi_0 + \varphi^\pi_1 - \varphi^\sigma_2$, where $\phi_0 = (\mathbf{k}_1 - \mathbf{k}_2) \cdot \hat{\mathbf{x}} = k_R d_x \cos(\theta)$ gives rise to the magnetic flux penetrating the side plaquette of the tube, with k_R the recoil momentum of the Raman lasers. Similarly, we have $\phi_{j;32} = j\phi_0 + \varphi^\sigma_2 - \varphi^\pi_3$, $\phi_{j;13} = -2j\phi_0 + \varphi^\sigma_3 - \varphi^\sigma_1$. To obtain a uniform magnetic flux for each side plaquette of the tube, we choose the incident angle θ such that the magnetic flux for each side plaquette is $\phi_0 = 2\pi/3$. The phases $\varphi^{\sigma,\pi}_s$ determine the flux through the tube, which is $\Phi \equiv -\phi_{j;21} - \phi_{j;32} - \phi_{j;13} = \varphi^\sigma_3 - \varphi^\pi_3 + \varphi^\pi_3 - \varphi^\sigma_3$. Therefore we obtain $\Phi = \Delta\varphi_3 - \Delta\varphi_1$, where $\Delta\varphi_s = \varphi^\pi_s - \varphi^\sigma_s$ is the phase difference between two polarization components of the sth Raman laser. We notice that the phase of each Raman coupling (i.e., $\phi_{j;ss'}$) depends on random phase difference between two Raman lasers (e.g., $\phi_{j;21}$ depends on $\varphi^\pi_1 - \varphi^\sigma_2$); however, their summation (i.e., the flux Φ) only depends on the phase difference $\Delta\varphi_s$ between two polarizations of the same Raman laser, which can be controlled at will using wave plates. Moreover, the phase differences $\Delta\varphi_s$ do not depend on the transverse positions y and z. Basically, the reason why we can control the flux Φ is that each spin state is dressed by one and only one Raman laser, and the random global phases of the Raman lasers can be gauged out by absorbing it into the definition of the spin states. With proper gauge choice, we can set the tunneling phases as $\phi_{j;21} = \phi_{j;32} = j\phi_0$ and $\phi_{j;13} = j\phi_0 + \Phi$, as shown in Fig. 1(d).

For alkali atoms, we choose $\mathcal{E}^\sigma_2 = 0$, yielding $\widetilde{\Omega}_{21;j} = \alpha_{21} \mathcal{E}^\sigma_1 \mathcal{E}^{\pi *}_2$, $\widetilde{\Omega}_{32;j} = \alpha_{32} \mathcal{E}^\pi_2 \mathcal{E}^{\pi *}_3$, and $\widetilde{\Omega}_{13;j} = \beta_{13} \mathcal{E}^\pi_3 \mathcal{E}^{\sigma *}_1 + \alpha_{13} \mathcal{E}^\sigma_3 \mathcal{E}^{\pi *}_1$, with $\alpha_{s,s'}, \beta_{s,s'}$ determined by the transition dipole matrix. We further consider $(\mathcal{E}^\pi_3, \mathcal{E}^\sigma_1) \ll (\mathcal{E}^\sigma_3, \mathcal{E}^\pi_1) \ll \mathcal{E}^\pi_2$ and $\mathcal{E}^\sigma_3 \mathcal{E}^\pi_1 \simeq \mathcal{E}^\pi_3 \mathcal{E}^\pi_2 \simeq \mathcal{E}^\sigma_1 \mathcal{E}^\pi_2$. Therefore we have $\widetilde{\Omega}_{13;j} \simeq \alpha_{13} \mathcal{E}^{\pi *}_1 \mathcal{E}^\sigma_3$ with amplitudes $\Omega_{21} \simeq \Omega_{32} \simeq \Omega_{13}$. Similar to the alkaline-earth(-like) atoms, we obtain uniform magnetic flux $\phi_0 = 2\pi/3$ for the tube side by choosing $k_R d_x \cos(\theta) = 2\pi/3$. The flux through the tube becomes $\Phi = \Delta\varphi_3 + \Delta\varphi_1$, which can also be tuned at will through the polarization control.

III. PHASE DIAGRAM

The Bloch Hamiltonian in the basis $[c_{k,1}, c_{k,2}, c_{k,3}]^T$ reads

$$H_k = \begin{bmatrix} -2J\cos(k - \phi_0) & \Omega_{21} & \Omega_{13} e^{-i\Phi} \\ \Omega_{21} & -2J\cos(k) & \Omega_{32} \\ \Omega_{13} e^{i\Phi} & \Omega_{32} & -2J\cos(k + \phi_0) \end{bmatrix}, \quad (2)$$

with k the momentum along the real-space lattice. For $\Omega_{21} = \Omega_{32} = \Omega_{13}$, the above Hamiltonian is nothing but the Harper-Hofstadter Hamiltonian, with Φ the effective momentum along the synthetic dimension, and $\phi_0 = 2\pi/3$ is the flux per plaquette. The topology is characterized by the Chern number [47]

$$C_n = \frac{i}{2\pi} \int dk d\Phi \langle \partial_\Phi u_n | \partial_k | u_n \rangle - \langle \partial_k u_n | \partial_\Phi | u_n \rangle, \quad (3)$$

where $|u_n\rangle$ is the Bloch state of the nth band, satisfying $H_k(\Phi)|u_n(\Phi, k)\rangle = E_n(\Phi, k)|u_n(\Phi, k)\rangle$. In Fig. 2(a), we plot the band structures as a function of Φ with an open boundary condition along the real-lattice direction. There are three bands and two gapless edge states (one at each end) in each

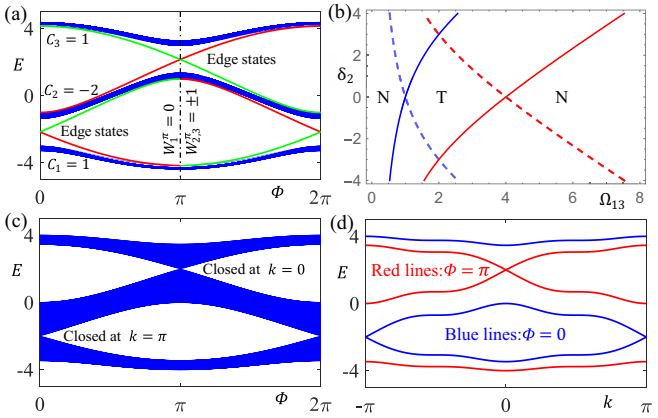

FIG. 2. (a) Band structures in the topological phase. (b) Phase diagram in the Ω_{13}-δ_2 plane, with solid (dashed) lines the boundary between topological (T) and normal (N) phases for the upper (lower) gap. (c), (d) Band structures at the left phase boundary with $\delta_2 = 0$ and $\Omega_{13} = 1$. Common parameters: $\Omega = 2$ with energy unit J.

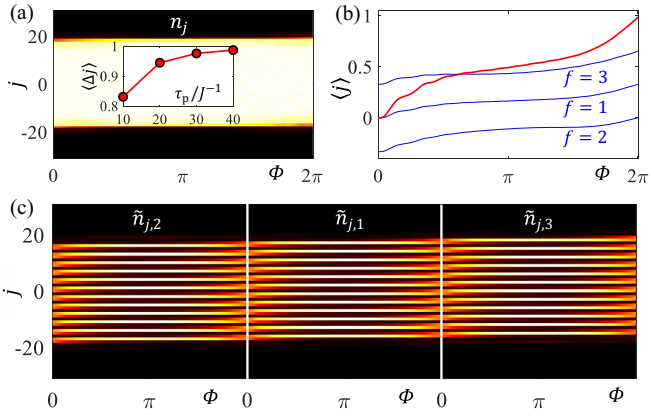

FIG. 3. (a) Total density distribution during one pump cycle. Inset shows the nonadiabatic effects on the center-of-mass shift. (b) Center-of-mass (red line) and the rotated-spin contributions (blue lines) during one pump cycle. The blue lines are $\sum_j j\tilde{n}_{j,f}(t)/N$ with $f = 1, 2, 3$ as labeled. (c) Rotated spin-density distributions during one pump cycle.

gap. The two edge states cross only at $\Phi = 0$ and $\Phi = \pi$, where the tube belongs to a 1D topological insulator with quantized winding number (Zak phase) [48]

$$W_n^{0,\pi} = \frac{1}{\pi} \oint dk \langle u_n | \partial_k | u_n \rangle |_{\Phi=0,\pi}. \tag{4}$$

The winding number is protected by a generalized inversion symmetry $\mathcal{I} H_k \mathcal{I}^{-1} = H_{-k}$, where the inversion symmetry $\mathcal{I}$ swaps spin states $|1\rangle$ and $|3\rangle$ [49].

The Chern number and winding number are still well defined, even when the Raman couplings have detunings and/or the coupling strengths $\Omega_{ss'}$ are nonequal. The changes in these Raman coupling parameters drive the phase transition from topological to trivial insulators. The detuning can be introduced by including additional terms $\sum_{j;s} \delta_s c_{j,s}^\dagger c_{j,s}$ in the Hamiltonian Eq. (1). Hereafter we will fix $\Omega_{21} = \Omega_{32} \equiv \Omega$ and $\delta_1 = \delta_3 = 0$ for simplicity. The phase diagram in the Ω_{13}-δ_2 plane is shown in Fig. 2(b). The solid (dashed) lines are the phase boundaries corresponding to the gap closing between two lower (upper) bands, with topological phases between two boundaries. At the phase boundaries, the corresponding band gaps close at $\Phi = 0$ ($\Phi = \pi$) for the two lower (upper) bands, as shown in Fig. 2(c). In addition, for the two lower (upper) bands, the gap closes at $k = 0$ and $k = \pi$ ($k = \pi$ and $k = 0$) on the right and left boundaries, respectively, as shown in Fig. 2(d). The gaps reopen in the trivial phase with the disappearance of edge states.

IV. TOPOLOGICAL PUMPING

The three-leg Hall tube is a minimal Laughlin cylinder. When the flux through the tube is adiabatically changed by 2π, the shift of Wannier-function center is proportional to the Chern number of the corresponding band [40–43]. Therefore all particles are pumped by C site (with C the total Chern number of the occupied bands) as Φ changes by 2π, i.e., C particles are pumped from one edge to another. Given the ability of controlling the flux through the tube, we can measure the topological Chern number based on topological pumping by tuning the flux Φ adiabatically (compared to the band gaps).

Here we consider the Fermi energy in the first gap with only the lowest $C = 1$ band occupied and study the zero-temperature pumping process (the pumped particle is still well quantized for low temperature comparing to the band gap) [50]. The topological pumping effect can be identified as the quantized center-of-mass shift of the atom cloud [50–53] in a weak harmonic trap $V_{\text{trap}} = \frac{1}{2} v_T j^2$. The harmonic trap strength $v_T = 0.008J$ and the atom number $N = 36$ are chosen such that the atom cloud has a large insulating region with one atom per unit cell at the trap center. (In a realistic experiment, the above parameters are typical.) For simplicity, we set $\Omega_{ss'} = J$ and $\delta_s = 0$ for all s, s', choose the gauge as $\phi_{j;21} = \phi_{j;32} = j\phi_0$, $\phi_{j;13} = j\phi_0 - \Phi$, and change Φ slowly (compared to the band gap) as $\Phi(t) = \frac{2\pi t}{\tau_p}$. In Figs. 3(a) and 3(b), we plot the total density distribution $n_j(t)$ and the center-of-mass $\langle j(t) \rangle \equiv \sum_j j n_j(t)/N$ shift during one pumping circle with $\tau_p = 40J^{-1}$, and we clearly see the quantization of the pumped atom $\langle \Delta j \rangle \equiv \langle j(\tau_p) \rangle - \langle j(0) \rangle = 1$. The atom cloud shifts as a whole with $n_j(t) = 1$ near the trap center. The inset in Fig. 3(a) shows a nonadiabatic effect (finite pumping duration τ_p) on the pumped atom. Typically, $J/2\pi$ is about several hundred Hertz; therefore the pumping duration τ_p should be of the order of tens of milliseconds to satisfy the adiabatic condition. This timescale is of the same magnitude as the lattice loading and time-of-flight imaging duration [34,35]. Starting from a degenerate Fermi gas prepared at the optical dipole trap, the whole experimental duration is less than 1 s (which is typical for cold atom experiments).

The atoms are equally distributed on the three spin states [i.e., $n_{j,s}(t) \equiv \langle c_{j,s}^\dagger c_{j,s} \rangle = \frac{1}{3} n_j(t)$]. To see the pumping process more clearly, we can examine the spin densities in the rotated basis $\tilde{n}_{j,f}(t) \equiv \langle \tilde{c}_{j,f}^\dagger \tilde{c}_{j,f} \rangle$, with $\tilde{c}_{j,f} = \frac{1}{\sqrt{3}} \sum_s c_{j,s} e^{is\frac{2f\pi - \Phi}{3}}$. The Hamiltonian in these basis reads $H = \sum_{f=1}^3 H_f$, where

$$H_f = 2J \cos(K_{j,f,\Phi}) \tilde{c}_{j,f}^\dagger \tilde{c}_{j,f} + (J \tilde{c}_{j,f}^\dagger \tilde{c}_{j,f+1} + \text{H.c.}) \tag{5}$$

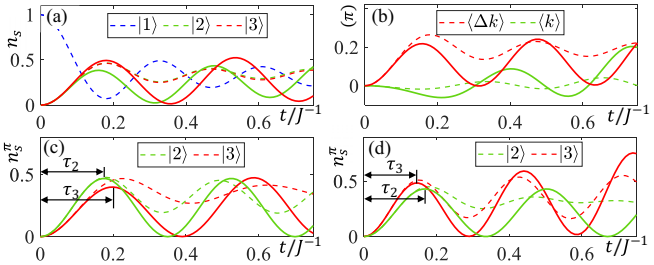

FIG. 4. Quench dynamics for $\Phi = 0$ (solid lines) and averaged over random Φ (dashed lines). Time evolution of spin populations (a) and averaged momenta (b) with $\Omega_{13} = \Omega$. Time evolution of spin populations at $k = \pi$ with $\Omega_{13} = 5$ in (c) and $\Omega_{13} = 7.5$ in (d). $n_s^\pi = \frac{n_s(\pi)}{\sum_{s'} n_{s'}(\pi)}$, τ_2 and τ_3 cross at $\Omega_{13}^c = 5.8$. Both gaps are topological in (a) and (b), and only the upper (lower) gap is topological in (c) [(d)]. Common parameters: $\Omega = 6.15$, $\delta_2 = -0.4\Omega$ with energy unit J.

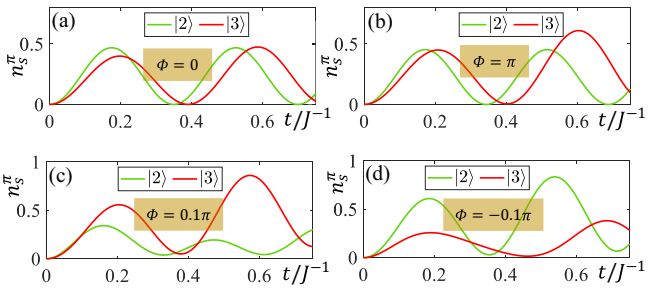

FIG. 5. (a)–(d) Time evolution of the spin populations at $k = \pi$ for different values of Φ. All other parameters are the same as Fig. 4(c).

is the typical Aubry-André-Harper (AAH) Hamiltonian [54,55] with $K_{j,f,\Phi} = \frac{2\pi(f+j)-\Phi}{3}$. Each spin component contributes exactly one-third of the quantized center-of-mass shift [see Fig. 3(b)]. The bulk-atom flow during the pumping can be clearly seen from the spin densities $\widetilde{n}_{j,f}(t)$, as shown in Fig. 3(c). The quantized pumping can also be understood by noticing that the AAH Hamiltonians H_s are permutated as $H_1 \to H_3 \to H_2 \to H_1$ after one pump circle. Each H_f returns to itself after three pump circles with particles pumped by three sites (since the lattice period of H_f is 3). Therefore for the total Hamiltonian H, particles are pumped by one site after one pump circle. The physics for different values of $\Omega_{ss'}$ and δ_s are similar, except that the rotated basis $\widetilde{c}_{j,f}$ may take different forms.

In the presence of atom-atom interactions, the robust topological properties should not be affected if the interaction strength is much weaker compared to the band gaps, and the charge pumping should remain quantized [56]. The interaction can be written as $H_{\rm int} = \frac{U}{2}\sum_{j,s\neq s'} \hat{n}_{j,s}\hat{n}_{j,s'}$ with atom number operator $\hat{n}_{j,s} = c_{j,s}^\dagger c_{j,s}$ and interaction strength U. The atom in site (j, s) would interact with atoms in all other sites $(j, s' \neq s)$ along the synthetic dimension. Therefore the interaction is long ranged along the synthetic dimension. At the strong interaction region, the system may produce fractional quantum Hall physics and support fractional topological pumping [44,45]. Our scheme generates a tunable flux through the tube and thus offers an ideal platform for studying quantized fractional charge transport and probing the fractional many-body Chern numbers.

V. QUENCH DYNAMICS

Besides topological pumping, the quench dynamics of the system can also be used to demonstrate the presence of gauge field ϕ_0 and detect the phase transitions [37]. Here we study how Φ affects the quench dynamics by considering that all atoms are initially prepared in state $|1\rangle$, and then the interleg couplings are suddenly activated by turning on the Raman laser beams. In Figs. 4(a) and 4(b) we show the time evolution of the fractional spin populations $n_s = \frac{1}{N}\int dk n_s(k)$, as well as the momenta $\langle k\rangle = \sum_s \langle k_s\rangle$ and $\langle \Delta k\rangle = \langle k_2\rangle - \langle k_3\rangle$ (both can be measured by time-of-flight imaging) for $\Phi = 0$, where $n_s(k) = \langle c_s(k)^\dagger c_s(k)\rangle$ and $\langle k_s\rangle = \frac{1}{N}\int k n_s(k) dk$ with N the total atom number. We find that the time evolutions show similar oscillating behaviors for different Φ, but with different frequencies and amplitudes. The difference between the momenta of atoms transferred to states $|2\rangle$ and $|3\rangle$ increase noticeably at early time as a result of the magnetic flux ϕ_0 penetrating the surface of the tube [37], which does not depend on the flux Φ through the tube. In Fig. 4 we have fixed $\Omega = 6.15J$, $\delta_2 = -0.4\Omega$, and $U = 0$. The initial temperature is set to be $T/T_F = 0.3$, with initial Fermi temperature T_F given by the difference between the Fermi energy E_F and the initial band minimum $-2J$ (i.e., $T_F = E_F + 2J$). We use $T_F = 2J$ to get the similar initial filling and Fermi distribution as those in the experiment [37] (the results are insensitive to T_F).

The quench dynamics can also be used to measure the gap closing at phase boundaries. Similar to Ref. [37], we introduce two times τ_2 and τ_3, at which the spin-$|2\rangle$ and spin-$|3\rangle$ populations at $k = 0$ (or $k = \pi$) reach their first maxima, to identify the phase boundary. As we change δ_2 or Ω_{13} across the phase boundary (one gap closes and the dynamics is characterized by a single frequency), τ_2 and τ_3 cross each other. Notice that the above discussions only apply to $\Phi = 0, \pi$ where the gap closing occurs. We find that even when no gap closing occurs for Φ away from 0 and π, τ_2 and τ_3 would cross each other as we increase Ω_{13}, and the crossing point is generally away from the phase boundaries. Therefore the measurement of gap closing based on quench dynamics is possible only if Φ can be controlled. As an example, we consider $\Phi = 0$ and plot the time evolution of the spin populations at $k = \pi$ with Ω_{13} around the left phase boundary Ω_{13}^c, as shown in Figs. 4(c) and 4(d). The crossing points are different for different Φ. In Fig. 5 we plot the time evolution of the spin populations at $k = \pi$ for different values of Φ.

The ability to control the flux Φ is crucial for the study of both topological properties and quench dynamics. We notice that for the experiment in [37], Φ cannot be controlled and may vary from one experimental realization to another, and Φ is also different for different tubes within one experimental realization. It is straightforward to show that the flux Φ in [37] is determined by the difference between the random phases of the Raman lasers at lattice sites (see Appendix), which cannot be controlled since the Raman lasers propagate along different paths, not to mention that their wavelengths are generally not

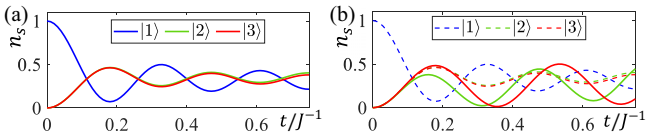

FIG. 6. Quench dynamics in the presence of a harmonic trap $V_{\rm trap} = \frac{1}{2}v_{\rm T}j^2$ for noninteracting fermions ($U = 0$) in (a) and interacting fermions ($U = 1.7J$) in (b). The trap strength is $v_{\rm T} \simeq 0.0158J$. The results in (a) are averaged over Φ. The solid (dashed) lines in (b) are the results for $\Phi = 0$ (averaged over Φ). All other parameters are the same as in Fig. 4(a).

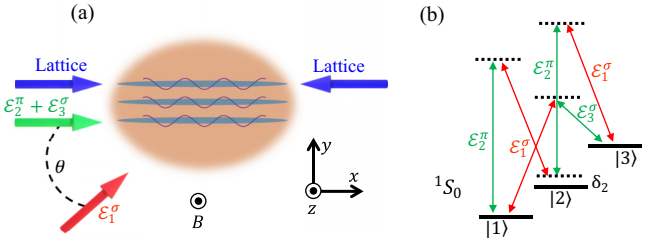

FIG. 7. (a) Schematic of the experimental setup and (b) the corresponding Raman transitions in [37].

commensurate with the lattice. Moreover, in realistic experiments, arrays of independent fermionic synthetic tubes are realized simultaneously due to the transverse atomic distributions in the y, z directions [36,37], and the synthetic tubes at different y would have different Φ due to the y-dependent φ_1^σ. For the parameters in Ref. [37], the difference of Φ between neighbor tubes in y direction is about $2\pi \times 0.58$. The random flux or phase problem is a common issue for schemes in which one spin state is dressed by two or more different lasers (different in wave vector) where the random global phases of the Raman lasers cannot be gauged out.

Due to the randomness of Φ, the dynamics in experiment [37] (averaged over enough samplings) should correspond to results averaged over Φ. In Fig. 4 we plot the corresponding dynamics averaged over Φ, which show damped oscillating behaviors (with significant long-time damping), as observed in the experiment. τ_2 and τ_3, which cross each other at different values of Ω_{13} for different Φ with averaged value $\bar{\Omega}_{13} = \Omega \neq \Omega_{13}^c$, may not be suitable to identify the phase boundaries (i.e., gap closings) for a random flux Φ.

In realistic experiments, a harmonic trap is usually applied to confine the atoms. The above results for the quench dynamics still hold for atoms in a weak harmonic trap, as confirmed by our numerical simulations. We consider a harmonic trap frequency $\omega_x = 2\pi \times 57$ Hz and $J = 2\pi \times 264$ Hz as in the experiment [37]; therefore the harmonic trap $V_{\rm trap} = \frac{1}{2}v_{\rm T}\ j^2$ has trap strength $v_{\rm T} \simeq 0.0158J$. In Fig. 6(a) we plot the time evolution of spin populations; we see that the quench dynamics are hardly affected by the harmonic trap. Moreover, atom-atom interactions may induce scattering between different momentum states that oscillate at different frequencies, leading to additional damping, which should be minor due to the short evolution time $\lesssim 1$ ms here. In Fig. 6(b) we plot the time evolution of spin populations in the presence of weak interaction $U = 1.7J$ [37]. We have adopted the mean-field approach and written the interaction as $\frac{U}{2}\sum_{j,s\neq s'}\hat{n}_{j,s}\hat{n}_{j,s'} = \frac{U}{2}\sum_{j,s\neq s'}[\langle\hat{n}_{j,s'}\rangle\hat{n}_{j,s} + \langle\hat{n}_{j,s}\rangle\hat{n}_{j,s'} - \langle\hat{n}_{j,s}\rangle\langle\hat{n}_{j,s'}\rangle]$, where the s-spin fermions interact with the average density of the s'-spin fermions, which should be valid for weak interaction and short evolution times (similar to the Hartree approximation). The weak interaction can hardly affect the quench dynamics where the oscillation frequency ($\sim\Omega$) is much larger than the interaction strength. Other experimental imperfections, such as spin-selective imaging error, may also affect the measured spin dynamics, and the final observed cross point in [37] is smaller than Ω and Ω_{13}^c.

VI. CONCLUSION

In summary, we propose a simple and feasible scheme to realize a controllable flux Φ through the synthetic Hall tube that can be tuned at will and study the effects of the flux Φ on the system topology and dynamics. Previous experimental quench dynamics may be better explained by the results averaged over the random flux existing in the experiment. Our scheme allows the study of interesting charge transport (e.g., the interesting charge flow and transport for rotated spin states in our system) through topological pumping, which also probes the system topology. Moreover, it may open the possibility to study fractional charge pumping and probe the many-body Chern numbers of fractional quantum Hall state at strong interactions. Our results provide a platform for studying topological physics in a tube geometry with tunable flux and may be generalized with other synthetic degrees of freedom, such as momentum states [57–59] and lattice orbitals [60,61].

ACKNOWLEDGMENTS

X.W.L. and C.Z. are supported by AFOSR (FA9550-16-1-0387, FA9550-20-1-0220), NSF (PHY-1806227), and ARO (W911NF-17-1-0128). J.Z. is supported by the National Key Research and Development Program of China (2016YFA0301602).

APPENDIX: RANDOM FLUX Φ IN PREVIOUS EXPERIMENTS

We would like to emphasize that our proposed setup to generate a tunable flux through the synthetic tube is different from the setup in recent experimental work [37] (as shown in Fig. 7 for comparison). The Raman laser configurations (directions, polarizations and frequencies) as well as the involved Raman processes are different. It is straightforward to show that the flux Φ for the setup in Fig. 7 is $\Phi = 3\varphi_1^\sigma - 2\varphi_2^\pi - \varphi_3^\sigma$, which cannot be controlled since the Raman lasers propagate along different paths, not to mention that their wavelengths are generally not commensurate with the lattice. The random flux or phase problem is a common issue for schemes in which one spin state is dressed by two or more different lasers (different in wave vector) where the random global phases of the Raman lasers can not be gauged out. Moreover, in realistic experiments, arrays of independent fermionic synthetic

tubes are realized simultaneously due to the transverse atomic distributions in the y, z directions, and the synthetic tubes at different y would have different Φ due to the y-dependent φ_1^σ for the setup in Fig. 7.

[1] D. Jaksch and P. Zoller, The cold atom Hubbard toolbox, Ann. Phys. (Amsterdam) **315**, 52 (2005).

[2] I. Bloch, J. Dalibard, and W. Zwerger, Many-body physics with ultracold gases, Rev. Mod. Phys. **80**, 885 (2008).

[3] Y.-J. Lin, K. Jiménez-García, and I. B. Spielman, Spin-orbit-coupled Bose-Einstein condensates, Nature (London) **471**, 83 (2011).

[4] J.-Y. Zhang, S.-C. Ji, Z. Chen, L. Zhang, Z.-D. Du, B. Yan, G.-S. Pan, B. Zhao, Y.-J. Deng, H. Zhai, S. Chen, and J.-W. Pan, Collective Dipole Oscillations of a Spin-Orbit Coupled Bose-Einstein Condensate, Phys. Rev. Lett. **109**, 115301 (2012).

[5] C. Qu, C. Hamner, M. Gong, C. Zhang, and P. Engels, Observation of *Zitterbewegung* in a spin-orbit-coupled Bose-Einstein condensate, Phys. Rev. A **88**, 021604(R) (2013).

[6] S.-C. Ji, J.-Y. Zhang, L. Zhang, Z.-D. Du, W. Zheng, Y.-J. Deng, H. Zhai, S. Chen, and J.-W. Pan, Experimental determination of the finite-temperature phase diagram of a spin-orbit coupled Bose gas, Nat. Phys. **10**, 314 (2014).

[7] A. Olson, S. Wang, R. Niffenegger, C. Li, C. Greene, and Y. Chen, Tunable Landau-Zener transitions in a spin-orbit-coupled Bose-Einstein condensate, Phys. Rev. A **90**, 013616 (2014).

[8] P. Wang, Z. Yu, Z. Fu, J. Miao, L. Huang, S. Chai, H. Zhai, and J. Zhang, Spin-Orbit Coupled Degenerate Fermi Gases, Phys. Rev. Lett. **109**, 095301 (2012).

[9] L. Cheuk, A. Sommer, Z. Hadzibabic, T. Yefsah, W. Bakr, and M. Zwierlein, Spin-Injection Spectroscopy of a Spin-Orbit Coupled Fermi Gas, Phys. Rev. Lett. **109**, 095302 (2012).

[10] Z. Wu, L. Zhang, W. Sun, X. Xu, B. Wang, S. Ji, Y. Deng, S. Chen, X.-J. Liu, and J. Pan, Realization of two-dimensional spin-orbit coupling for Bose-Einstein condensates, Science **354**, 83 (2016).

[11] Z. Meng, L. Huang, P. Peng, D. Li, L. Chen, Y. Xu, C. Zhang, P. Wang, and J. Zhang, Experimental Observation of a Topological Band Gap Opening in Ultracold Fermi Gases with Two-Dimensional Spin-Orbit Coupling, Phys. Rev. Lett. **117**, 235304 (2016).

[12] L. Huang, Z. Meng, P. Wang, P. Peng, S. Zhang, L. Chen, D. Li, Q. Zhou, and J. Zhang, Experimental realization of two-dimensional synthetic spin-orbit coupling in ultracold Fermi gases, Nat. Phys. **12**, 540 (2016).

[13] L. Huang, P. Peng, D. Li, Z. Meng, L. Chen, C. Qu, P. Wang, C. Zhang, and J. Zhang, Observation of Floquet bands in driven spin-orbit-coupled Fermi gases, Phys. Rev. A **98**, 013615 (2018).

[14] S. Kolkowitz, S. L. Bromley, T. Bothwell, M. L. Wall, G. E. Marti, A. P. Koller, X. Zhang, A. M. Rey, and J. Ye, Spin-orbit-coupled fermions in an optical lattice clock, Nature (London) **542**, 66 (2017).

[15] S. L. Bromley, S. Kolkowitz, T. Bothwell, D. Kedar, A. Safavi-Naini, M. L. Wall, C. Salomon, A. M. Rey, and J. Ye, Dynamics of interacting fermions under spin-orbit coupling in an optical lattice clock, Nat. Phys. **14**, 399 (2018).

[16] D. Campbell, R. Price, A. Putra, A. Valdés-Curiel, D. Trypogeorgos, and I. B. Spielman, Magnetic phases of spin-1 spin-orbit-coupled Bose gases, Nat. Commun. **7**, 10897 (2016).

[17] X. Luo, L. Wu, J. Chen, Q. Guan, K. Gao, Z.-F. Xu, L. You, and R. Wang, Tunable atomic spin-orbit coupling synthesized with a modulating gradient magnetic field, Sci. Rep. **6**, 18983 (2016).

[18] A. Valdés-Curiel, D. Trypogeorgos, Q.-Y. Liang, R. P. Anderson, and I. B. Spielman, Unconventional topology with a Rashba spin-orbit coupled quantum gas, arXiv:1907.08637.

[19] J. Dalibard, F. Gerbier, G. Juzeliūnas, and P. Öhberg, Colloquium: Artificial gauge potentials for neutral atoms, Rev. Mod. Phys. **83**, 1523 (2011).

[20] N. Goldman, G. Juzeliūnas, P. Öhberg, and I. B. Spielman, Light-induced gauge fields for ultracold atoms, Rep. Prog. Phys. **77**, 126401 (2014).

[21] V. Galitski and I. B. Spielman, Spin-orbit coupling in quantum gases, Nature (London) **494**, 49 (2013).

[22] H. Zhai, Spin-orbit coupled quantum gases, Int. J. Mod. Phys. B **26**, 1230001 (2012).

[23] H. Zhai, Degenerate quantum gases with spin-orbit coupling: A review, Rep. Prog. Phys. **78**, 026001 (2015).

[24] J. Zhang, H. Hu, X.-J. Liu, and H. Pu, Fermi gases with synthetic spin–orbit coupling, Annu. Rev. Cold At. Mol. **2**, 81 (2014).

[25] D.-W. Zhang, Y.-Q. Zhu, Y. X. Zhao, H. Yan, and S.-L. Zhu, Topological quantum matter with cold atoms, Adv. Phys. **67**, 253 (2018).

[26] J. Struck, C. Ölschläger, M. Weinberg, P. Hauke, J. Simonet, A. Eckardt, M. Lewenstein, K. Sengstock, and P. Windpassinger, Tunable Gauge Potential for Neutral and Spinless Particles in Driven Optical Lattices, Phys. Rev. Lett. **108**, 225304 (2012).

[27] M. Aidelsburger, M. Atala, M. Lohse, J. T. Barreiro, B. Paredes, and I. Bloch, Realization of the Hofstadter Hamiltonian with Ultracold Atoms in Optical Lattices, Phys. Rev. Lett. **111**, 185301 (2013).

[28] H. Miyake, G. A. Siviloglou, C. J. Kennedy, W. C. Burton, and W. Ketterle, Realizing the Harper Hamiltonian with Laser-Assisted Tunneling in Optical Lattices, Phys. Rev. Lett. **111**, 185302 (2013).

[29] O. Boada, A. Celi, J. I. Latorre, and M. Lewenstein, Quantum Simulation of an Extra Dimension, Phys. Rev. Lett. **108**, 133001 (2012).

[30] A. Celi, P. Massignan, J. Ruseckas, N. Goldman, I. B. Spielman, G. Juzeliūnas, and M. Lewenstein, Synthetic Gauge Fields in Synthetic Dimensions, Phys. Rev. Lett. **112**, 043001 (2014).

[31] H. M. Price, O. Zilberberg, T. Ozawa, I. Carusotto, and N. Goldman, Four-Dimensional Quantum Hall Effect with Ultracold Atoms, Phys. Rev. Lett. **115**, 195303 (2015).

[32] C.-H. Li, Y. Yan, S. Choudhury, D. B. Blasing, Q. Zhou, and Y. P. Chen, A Bose-Einstein condensate on a synthetic Hall cylinder, arXiv:1809.02122.

[33] Y. Yan, S.-L. Zhang, S. Choudhury, and Q. Zhou, Emergent Periodic and Quasiperiodic Lattices on Surfaces of Synthetic Hall Tori and Synthetic Hall Cylinders, Phys. Rev. Lett. **123**, 260405 (2019).

[34] M. Mancini, G. Pagano, G. Cappellini, L. Livi, M. Rider, J. Catani, C. Sias, P. Zoller, M. Inguscio, M. Dalmonte, and L.

Fallani, Observation of chiral edge states with neutral fermions in synthetic Hall ribbons, Science **349**, 1510 (2015).

[35] B. K. Stuhl, H.-I. Lu, L. M. Aycock, D. Genkina, and I. B. Spielman, Visualizing edge states with an atomic Bose gas in the quantum Hall regime, Science **349**, 1514 (2015).

[36] L. F. Livi, G. Cappellini, M. Diem, L. Franchi, C. Clivati, M. Frittelli, F. Levi, D. Calonico, J. Catani, M. Inguscio, and L. Fallani, Synthetic Dimensions and Spin-Orbit Coupling with an Optical Clock Transition, Phys. Rev. Lett. **117**, 220401 (2016).

[37] J. H. Han, J. H. Kang, and Y. Shin, Band Gap Closing in a Synthetic Hall Tube of Neutral Fermions, Phys. Rev. Lett. **122**, 065303 (2019).

[38] R. P. Anderson, D. Trypogeorgos, A. Valdés-Curiel, Q.-Y. Liang, J. Tao, M. Zhao, T. Andrijauskas, G. Juzeliūnas, and I. B. Spielman, Realization of a deeply subwavelength adiabatic optical lattice, Phys. Rev. Research **2**, 013149 (2020).

[39] D. R. Hofstadter, Energy levels and wave functions of Bloch electrons in rational and irrational magnetic fields, Phys. Rev. B **14**, 2239 (1976).

[40] R. B. Laughlin, Quantized Hall conductivity in two dimensions, Phys. Rev. B **23**, 5632 (1981).

[41] D. J. Thouless, Quantization of particle transport, Phys. Rev. B **27**, 6083 (1983).

[42] Q. Niu, Towards a Quantum Pump of Electric Charges, Phys. Rev. Lett. **64**, 1812 (1990).

[43] D. Xiao, M.-C. Chang, and Q. Niu, Berry phase effects on electronic properties, Rev. Mod. Phys. **82**, 1959 (2010).

[44] T.-S. Zeng, C. Wang, and H. Zhai, Charge Pumping of Interacting Fermion Atoms in the Synthetic Dimension, Phys. Rev. Lett. **115**, 095302 (2015).

[45] L. Taddia, E. Cornfeld, D. Rossini, L. Mazza, E. Sela, and R. Fazio, Topological Fractional Pumping with Alkaline-Earth-Like Atoms in Synthetic Lattices, Phys. Rev. Lett. **118**, 230402 (2017).

[46] M. Boyd, T. Zelevinsky, A. Ludlow, S. Blatt, T. Zanon-Willette, S. Foreman, and J. Ye, Nuclear spin effects in optical lattice clocks, Phys. Rev. A **76**, 022510 (2007).

[47] D. J. Thouless, M. Kohmoto, M. P. Nightingale, and M. den Nijs, Quantized Hall Conductance in a Two-Dimensional Periodic Potential, Phys. Rev. Lett. **49**, 405 (1982).

[48] J. Zak, Berry's Phase for Energy Bands in Solids, Phys. Rev. Lett. **62**, 2747 (1989).

[49] S. Barbarino, M. Dalmonte, R. Fazio, and G. E. Santoro, Topological phases in frustrated synthetic ladders with an odd number of legs, Phys. Rev. A **97**, 013634 (2018).

[50] L. Wang, M. Troyer, and X. Dai, Topological Charge Pumping in a One-Dimensional Optical Lattice, Phys. Rev. Lett. **111**, 026802 (2013).

[51] L. Wang, A. A. Soluyanov, and M. Troyer, Proposal for Direct Measurement of Topological Invariants in Optical Lattices, Phys. Rev. Lett. **110**, 166802 (2013).

[52] M. Lohse, C. Schweizer, O. Zilberberg, M. Aidelsburger, and I. Bloch, A Thouless quantum pump with ultracold bosonic atoms in an optical superlattice, Nat. Phys. **12**, 350 (2016).

[53] S. Nakajima, T. Tomita, S. Taie, T. Ichinose, H. Ozawa, L. Wang, M. Troyer, and Y. Takahashi, Topological Thouless pumping of ultracold fermions, Nat. Phys. **12**, 296 (2016).

[54] P. G. Harper, Single band motion of conduction electrons in a uniform magnetic field, Proc. Phys. Soc. London Sect. A **68**, 874 (1955).

[55] S. Aubry and G. André, Analyticity breaking and Anderson localization in incommensurate lattices, Ann. Isr. Phys. Soc. **3**, 133 (1980).

[56] Q. Niu and D. J. Thouless, Quantised adiabatic charge transport in the presence of substrate disorder and many-body interaction, J. Phys. A **17**, 2453 (1984).

[57] E. J. Meier, F. A. An, and B. Gadway, Observation of the topological soliton state in the Su-Schrieffer-Heeger model, Nat. Commun. **7**, 13986 (2016).

[58] F. A. An, E. J. Meier, and B. Gadway, Direct observation of chiral currents and magnetic reflection in atomic flux lattices, Sci. Adv. **3**, e1602685 (2017).

[59] F. A. An, E. J. Meier, and B. Gadway, Diffusive and arrested transport of atoms under tailored disorder, Nat. Commun. **8**, 325 (2017).

[60] H. M. Price, T. Ozawa, and N. Goldman, Synthetic dimensions for cold atoms from shaking a harmonic trap, Phys. Rev. A **95**, 023607 (2017).

[61] J. H. Kang, J. H. Han, and Y. Shin, Realization of a Cross-Linked Chiral Ladder with Neutral Fermions in a 1D Optical Lattice by Orbital-Momentum Coupling, Phys. Rev. Lett. **121**, 150403 (2018).